



High Speed In Situ Synchrotron Observation of Cyclic Deformation and Phase Transformation of Superelastic Nitinol at Ultrasonic Frequency

M. Fitzka¹ · H. Rennhofer¹ · D. Catoor² · M. Reiterer² · H. Lichtenegger¹ · S. Checchia^{3,4} · M. di Michiel³ · D. Irrasch¹ · T.A. Gruenewald³ · H. Mayer¹

Received: 30 May 2019 / Accepted: 21 October 2019 / Published online: 5 December 2019
© The Author(s) 2019

Abstract

The near equi-atomic intermetallic Ni Ti alloy Nitinol is used for medical implants, notably in self-expanding stent grafts and heart valve frames, which are subjected to several hundred million load cycles in service. Increasing the testing frequency to the ultrasonic range would drastically shorten the testing times and make the very-high cycle regime experimentally accessible. Such tests are, however, only meaningful if the material response at ultrasonic frequency is identical to that observed in conventional fatigue tests. A novel fatigue testing setup where superelastic Nitinol dog bone specimens are loaded at ultrasonic cycling frequency is presented. Loading conditions resemble in vivo loading (i.e., repeated cyclic loading with relatively small strain amplitudes, specimens in a pre-strained multi-phase state). Strains and phase transformations during ultrasonic frequency cycling are quantitatively measured in an X-ray diffraction (XRD) synchrotron experiment and compared to the material response at low frequency. The XRD experiment confirms that forward and reverse stress-induced phase transformation from austenite to martensite via the intermediate R-phase occurs during low frequency (0.1 Hz, strain rate $\dot{\epsilon} \approx 10^{-3} \text{ s}^{-1}$) and ultrasonic frequency (20 kHz, $\dot{\epsilon} \approx 10^2 \text{ s}^{-1}$) cycling. Since the same deformation mechanisms are active at low and ultrasonic frequency, these findings imply a general applicability of the ultrasonic fatigue testing technique to Nitinol.

Keywords Shape memory alloy · Biomedical materials · Ultrasonic cycling · X-ray diffraction

Nomenclature

DAQ	Data acquisition.
DIC	Digital image correlation.
ESRF	European Synchrotron Radiation Facility.
FEA	Finite Element Analysis.
FWHM	Full width at half maximum.
HCF	High cycle fatigue.
USF	Ultrasonic fatigue testing.
VHCF	Very-high cycle fatigue.

XRD	X-ray diffraction.
A_f	Austenite finish temperature ($^{\circ}\text{C}$).
d	Lattice spacing (\AA)
Δd	Lattice deformation (\AA)
Q	Scattering vector (\AA^{-1}) where $Q = 4\pi/\lambda \cdot \sin(\theta)$ with wavelength λ (\AA) of the incident X-ray beam and θ half the scattering angle 2θ
ϵ_g	Global strain calculated from the extension of the specimen fixtures under tensile load
$\Delta\epsilon/2$	strain amplitude due to the cyclic displacement amplitude $\Delta u/2$
$\dot{\epsilon}$	Strain rate (s^{-1})
$\epsilon_{\min}, \epsilon_{\max}$	Minimum (maximum) tensile strain during one ultrasonic cycle
ϕ	Phase of the sinusoidal ultrasonic vibration ($^{\circ}$)
$\Delta\phi_{\text{fwm}}$	Frame phase window ($^{\circ}$)
$\Delta\phi_i$	Phase offset along the ultrasonic vibration signal ($^{\circ}$)
$\Delta\phi_{\epsilon_{\max}}$	Phase offset along the ultrasonic vibration signal at which minimum strain is reached ($^{\circ}$)

✉ M. Fitzka
michael.fitzka@boku.ac.at

¹ Institute of Physics and Materials Science, University of Natural Resources and Life Sciences, Vienna, Austria

² Medtronic Inc., Core Technologies, Corporate Science and Technology, Minneapolis, MN, USA

³ European Synchrotron Radiation Facility, Grenoble, France

⁴ MAX IV Laboratory, Lund University, 22100 Lund, Sweden

$\Delta\phi_{\varepsilon_{\min}}$	Phase offset along the ultrasonic vibration signal at which minimum strain is reached ($^{\circ}$)
$\Delta u/2$	Cyclic displacement amplitude (μm)

Introduction

Since its discovery in 1962 [1, 2], the nearly equi-atomic intermetallic Ni-Ti alloy, commonly known as Nitinol, has attracted much interest for industrial applications. Presently, it is widely used in the medical device industry [3, 4] because of its two unique and closely related properties of shape memory effect and superelasticity [5, 6], as well as excellent corrosion resistance, biocompatibility, and fatigue resistance [7, 8]. Common applications are minimally invasive implants like stents, stent grafts and heart valve frames [3, 4, 9–11].

Superelasticity and shape memory in Nitinol are due to a reversible stress-induced martensitic transformation from B2 austenite to a B19' martensite, often via an intermediate rhombohedral phase called the R-phase [12]. Both the forward and reverse transformation proceed at near constant stresses that are commonly referred to as the upper and lower plateau stresses, respectively. This reversible phase transformation enables Nitinol devices to be compressed into a small diameter catheter, transported to the implant location and released, whereupon they “self-expand” i.e., regain their shape, to perform the intended function of structural support to blood vessels and heart valves. During compression into a catheter, the forward transformation from austenite to martensite occurs in high-stress regions of the component; and during self-expansion, spontaneous reverse transformation from martensite to austenite occurs. Because these devices are designed to prevent constriction of vessels, they are required to apply an outward force and are not unloaded completely. So, the reverse transformation is restricted, leading to a multi-phase composite comprising austenite, R-phase and martensite in the implant condition. This composite is subjected to predominantly displacement-controlled cyclic loading by the surrounding tissue, resulting from cardiac cycles or musculoskeletal movements.

Long term implants like heart valve frames and stents must withstand very large numbers of load cycles. Assuming a typical adult human heart rate of 72 beats per minute, 15 years of implant life will roughly yield 5×10^8 cycles. Consequently, fatigue properties of Nitinol in the very-high cycle fatigue (VHCF) regime are of great interest, as these data are essential for the development and introduction of Nitinol-based medical devices. However, several difficulties are associated with the investigation in the VHCF regime. First, the testing method must reproduce the multi-phase state (austenite, R-phase, martensite) present in implants in vivo after the implant procedure. VHCF lifetimes will, for example, not occur in fully reversed fatigue tests, where specimens

undergo entire transformation cycles and will fail early. Specimens in a multi-phase state, however, can behave entirely differently, as Nitinol exhibits a strong dependency of lifetimes on mean strain (e.g., [13]), where the interaction between material phases and crack initiation and propagation play a governing role. A limiting factor for very-high cycle fatigue testing is the long testing time associated with conventional testing methods, e.g. of thin wires and diamond shaped specimens [9, 14–16]. Hence, testing of devices is time consuming, and precludes fast material selection and/or design iterations. Within the context of understanding material behavior, samples are often not tested to failure, but are taken off the test at 10^7 cycles, without the opportunity to investigate possible failures that may occur at greater numbers of cycles, which limits the available knowledge about the HCF and especially VHCF fatigue properties of Nitinol [6, 7, 10, 11].

Ultrasonic fatigue testing (USF) offers a faster alternative for obtaining HCF and VHCF data within reasonable testing times. Nitinol, however, has a strongly strain rate dependent deformation response. At quasi-static cyclic loading rates, elastic-plastic loading and phase transformation are both active in Nitinol [5], and both contribute to fatigue damage evolution and failure. It is not clear if the same deformation and damage mechanisms operate at ultrasonic loading rates. The stress-induced phase transformation in Nitinol is accompanied by a latent heat release that causes adiabatic heating which, in turn, leads to increased transformation stress. This manifests as rate-dependent mechanical response [17, 18]. At sufficiently high rates, the phase transformation could be suppressed [19]. In tension, the phase transformation is spatially heterogeneous and proceeds in a Luders-band like form [20]. In order for ultrasonic fatigue testing to be applicable to Nitinol, it is necessary to show that mechanisms of phase transformations and plastic deformations in ultrasonic and conventional loading rates are fundamentally identical. It is of great scientific and practical interest, if applications of Nitinol could benefit from this vastly accelerated testing technique.

Synchrotron X-ray diffraction, where lattice deformation and phase changes can both be measured in situ and with adequate spatial resolution, has been used by many researchers to investigate and shed new light on Nitinol mechanical behavior [21–25]. One could assess the viability of ultrasonic fatigue testing for Nitinol by acquiring in situ synchrotron XRD data if a sufficiently high sampling rate can be achieved to capture a 20 kHz load cycle and by comparing the deformation mechanisms with those that occur at ordinary rates.

In this study, we developed a novel experimental method for acquiring high-speed in situ XRD data during ultrasonic cycling of thin superelastic Nitinol sheets with sufficient fidelity for measuring cyclic strain and phase transformation. We applied small cyclic strains on Nitinol sheet-cut dog bones at a



non-zero mean strain where a multi-phase state was present, similar to the scenario encountered in implanted devices. The loading frequency was approximately 20 kHz, with corresponding strain rates between $5 \times 10^1 \text{ s}^{-1}$ and $4 \times 10^2 \text{ s}^{-1}$. We present the resulting synchrotron XRD data and discuss deformation and phase transformation behavior of Nitinol under these loading conditions. Subsequently, we evaluate ultrasonic fatigue loading as a method for ultrahigh cycle fatigue testing.

Cyclic Loading of Superelastic Nitinol at Ultrasonic Frequency

Material and Specimens

Superelastic Nitinol with 55.9 wt% nickel with an austenite finish temperature (A_f) of (13.4–14.5) °C was obtained from Johnson-Matthey (San Jose, CA, USA). Austenite is therefore stable at room and body temperature in the absence of stress. Tapered dog bone specimens of approximately 0.25 mm in thickness (Fig. 1, left) were laser cut, microblasted and electropolished by Laserage Technology Corporation (Waukegan, IL, USA). Microblasting and electropolishing were performed to remove the recast and heat affected material from laser machining, as is typically done in Nitinol medical implants. The enhanced surface finish improves fatigue performance.

Figure 2 shows a representative engineering stress-strain curve for the superelastic Nitinol specimens used in the present study, under displacement-controlled loading. Upon applying tensile stress, the austenitic (B2) phase deforms elastically, leading to linear behavior. At around 200 MPa the linearity is lost due to the formation of the R-phase (a

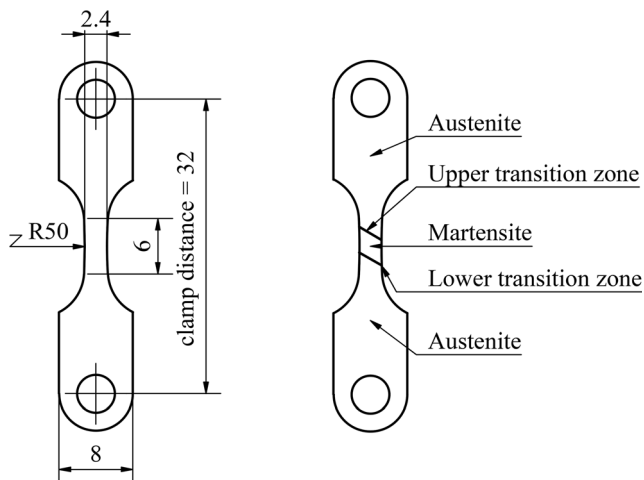


Fig. 1 Sheet specimen shape used for ultrasonic fatigue testing and in situ XRD (all dimensions in mm), specimen thickness is 0.25 mm (left); phase distribution across the pre-strained specimen (right)

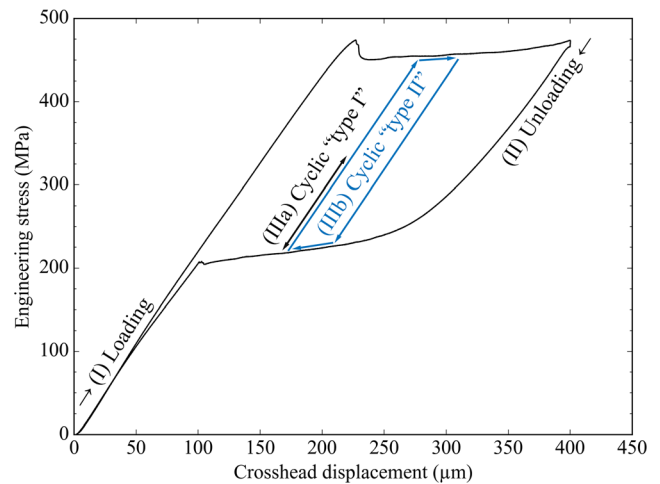


Fig. 2 Stress-strain curve of specimen pre-straining procedure applied before cyclic loading

rhombohedral distortion of the cubic B2 phase [26]). When the maximum stress in the center of the specimen reaches the temperature dependent forward transformation stress, the material transforms to martensite (B19'), that allows for continued deformation without a significant increase of stress (upper plateau stress). The visible increase is due to the taper in the specimen. As a single martensitic band grows from the narrowest cross section to an increasingly wider one, a greater load is required to reach the transformation stress (Fig. 1, right). When the specimen is unloaded, first the martensite relaxes elastically, leading to a decrease in stress. When the reverse transformation stress is reached, the martensite begins to transform back to austenite at a nearly constant stress (lower plateau stress), recovering the transformation strain. With the transformation completed, the austenite unloads elastically.

Mechanical Setup for Synchrotron In Situ Cycling

Stents and similar medical devices are first compressed into a catheter, transported to the implant location through arteries and “deployed” by releasing from the catheter, which results in a multi-phase composite comprising austenite, martensite, and often the R-phase. During service, this composite is subject to cyclic loading. In the present study, a pre-strain is applied, which is the tensile equivalent of the above process as shown in Fig. 2: A global strain ϵ_g (i.e., extension of the clamp distance in Fig. 1, left) of approximately 6% is applied first to mimic compression into a catheter where forward transformation to martensite occurs; deployment i.e., releasing the device from the catheter, is equivalent to partially unloading the test specimen to reach $\approx 3\%$ global strain along the lower plateau where the reverse transformation to austenite is partially complete. Subsequent cyclic loading mimics pulsatile loading within the blood vessel due to cardiac cycles.

During “type I” loading (Fig. 2, IIIa) the specimen is cycled so that neither the upper plateau stress is exceeded, nor the lower plateau stress is undershot i.e., the specimen only experiences nominally elastic deformation. In “type II” (Fig. 2, IIIb) both plateau stresses are exceeded / undershot so that the specimen should undergo forward and reverse transformation between the austenitic B2 austenite phase and the B19’ martensite phase.

A miniaturized tensile stage to fit into the beam path at beamline ID15A at the ESRF was developed, that incorporates an ultrasonic load train (Fig. 3). With this, the specimen can be cyclically loaded in the synchrotron beam path at approximately 20 kHz after the simulated crimping procedure (Fig. 3, left). The tensile stage is equipped with a load cell of 500 N capacity. Two synchronously stepper motor driven spindles allow for 0.3 μm step resolution of crosshead displacement. The stage is controlled via custom software written in NATIONAL INSTRUMENTS LabVIEW and allows for displacement, load, and extension control. It also features a basic function generator for sinusoidal loading at frequencies up to 2 Hz.

Small Cyclic Strains at High Strain Rates

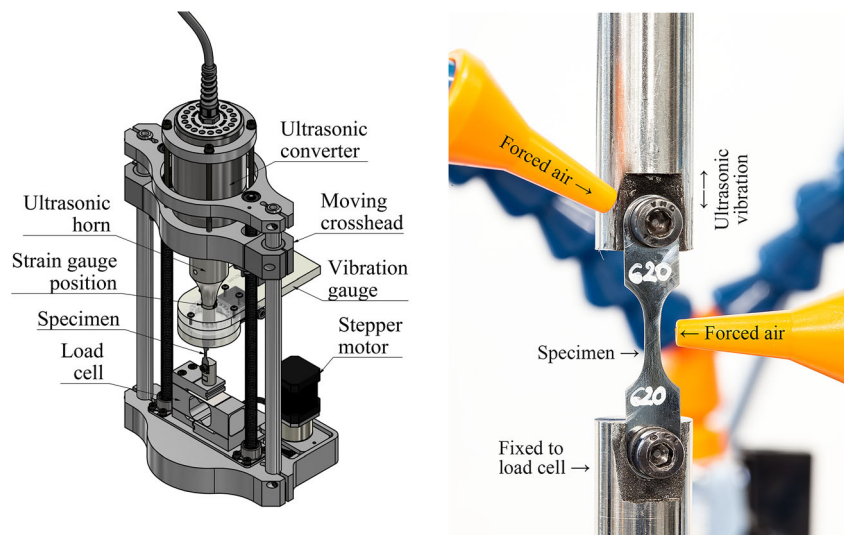
Cyclic loading of thin sheets at ultrasonic frequency is not trivial, as the specimen shape imposes significant constraints on existing ultrasonic fatigue testing techniques. For specimens of small thickness (typically below 1 mm thickness), sound transfer degrades and undesirable higher order harmonics could occur due to the abrupt change in cross section from the load train to the thin sheet. At the same time, the tendency of the specimen to buckle increases as sheet thickness decreases due to the decreasing critical buckling load. In an existing technique to test thin maraging steel sheets at ultrasonic frequency the sheet specimen is clamped to a so-

called carrier specimen and is forced to vibrate along with the resonance vibration of the carrier specimen [27]. This approach, however, is not directly applicable to thin sheets of Nitinol, as the carrier specimen cannot accommodate the large static strains that are required for the pre-straining procedure.

In the present investigation, we adapted the conventional ultrasonic fatigue testing method for cycling thin sheets of superelastic Nitinol by removing the resonance requirement altogether (Fig. 3). Rather, the upper end of the sheet specimen is screw-mounted to the lower end (i.e., vibration antinode) of a resonating ultrasonic horn. The lower end of the specimen is screw-mounted to a rigidly mounted rod stub at the load cell. The upper end of the specimen is thus forced to move in unison with the resonance vibration of the horn at approximately 20 kHz and is experiencing cyclic strain at the same frequency. The specimen is not vibrating in resonance, but it is cyclically stressed in a quasi-static fashion.

The sinusoidal cyclic displacement at about 20 kHz cycling frequency is generated and controlled by the ultrasonic fatigue testing equipment developed at Physics BOKU Vienna [28]. Specimen and fixture heating were avoided by the combined use of a pulse-pause sequence for loading and forced-air cooling (21 °C). Pulses of 100 ms and pauses of about 500 ms were found to be adequate. The displacement amplitude $\Delta u/2$ of the vibration antinode at the lower end of the ultrasonic horn (i.e., the upper end of the specimen) is obtained from dynamic strain gauge readings taken at the position indicated in Fig. 3, that are translated to displacement amplitudes $\Delta u/2$ via modal FEA simulation [29] at the actual resonance frequency of ≈ 18.3 kHz. The relationship between strain gauge reading and displacement of the horn’s lower end was verified with a FOTONIC fiber optic measurement system. The same sensor was intermittently employed to confirm that no buckling vibrations occurred.

Fig. 3 Mechanical setup for in situ synchrotron XRD during cycling at ultrasonic frequency; schematic (left) and detail view with mounted specimen (right)



Pre-Straining, DIC and Static Strain Distribution

The pre-straining procedure as well as cyclic loading were both performed under displacement control. Because of the localized nature of the transformation [20], strain is heterogeneous across the specimen and cannot be calculated analytically from the global load-displacement data. In addition, for a given static displacement or ultrasonic cyclic displacement, the resulting strains and strain amplitudes depend on the compliance of the system load frame, ultrasonic load train and the specimen. A relationship between applied displacements and strains within the dog bone can be obtained despite these difficulties by using a strain mapping technique like digital image correlation (DIC).

A DANTEC DYNAMICS DIC system was employed to derive global strain and the strain distribution along the specimen as a function of crosshead displacement. First, the specimen was loaded to approximately 6% global strain. A single martensite band nucleates at the center of the specimen at a 34° angle to the horizontal. As loading progresses, the entire gauge section of the specimen is converted to martensite. During the partial unload to 3% global strain, the band contracts back to the center, resulting in a single martensite band at the center of the gauge section and austenitic regions above and below this band (Fig. 1, right). The strain in the martensite band, a sum of both elastic and transformation strains, is 4% - 5%, whereas the strain in the austenitic region remains below 1%. R-phase is not detectable by DIC due to the small strains involved in the austenite to R-phase transformation and its continuous nature. The interface between austenite/R-phase and martensite, though visible as a sharp line on the surface to the naked eye, is revealed to be a narrow band of material ($100\ \mu\text{m}$ - $150\ \mu\text{m}$ width) with intermediate strains. This band is distinct from the martensitic band and will be referred to as the upper and lower transition zone, respectively (Fig. 1, right).

In Situ Synchrotron XRD during Ultrasonic Cycling

In situ synchrotron diffraction experiments were performed at the European Synchrotron Radiation Facility (ESRF) to investigate the material response at the very high strain rates during ultrasonic loading (between $10^1\ \text{s}^{-1}$ and $2 \times 10^2\ \text{s}^{-1}$). Of particular interest in this investigation is the equivalence of deformation mechanisms and phase transformation at low and ultrasonic frequency. To that end it must be verified that both, the R-phase as well as the martensitic phase, occur during cyclic loading at approximately 20 kHz as they do under quasi-static or low frequency loading conditions. XRD is a commonly used non-destructive technique for observing lattice deformation in a wide range of materials and has been successfully applied to Nitinol for phase identification

[30–32]. The present experiment aims to combine those abilities of XRD with in situ cyclic loading of Nitinol sheet specimens to resolve lattice deformations and phase transitions during cycling at ultrasonic frequency, resulting in small strains at high strain rates.

XRD Setup

The experiment was conducted at the ESRF in Grenoble, France, at the beamline ID15A, which was specifically chosen for its high-energy X-ray radiation and its fast detector capability (Vaughan, G.B.M, et al., J. Synchrotron Radiat., under review). It is crucial to achieve short exposure times (approximately $1\ \mu\text{s}$) so that the diffraction spectra corresponding to a specific phase ϕ of the sinusoidal 20 kHz vibration can be reliably recorded. 60 keV radiation was employed for all measurements in this study with a beam size of $(134 \pm 5)\ \mu\text{m} \times (170 \pm 5)\ \mu\text{m}$ FWHM. The sample to detector distance was 714 mm. The DECTRIS CdTe Pilatus 2 M detector used in this study is capable of very short gated exposures i.e., the detector will expose for as long as an external trigger signal remains at logic high level. The minimum successfully achieved exposure time was 170 ns, which comfortably permits the targeted exposure time of $1\ \mu\text{s}$. Sample-detector distance and Q -range were calibrated with a LaB_6 powder sample; the background was corrected with an air measurement of 40 min duration. Tests were carried out in air with a controlled temperature of $21\ ^\circ\text{C}$ at 50% relative humidity.

Data Acquisition Strategy

Preliminary tests at ID15A had indicated that with an energy of 60 keV, exposure times of about 10 ms were necessary to acquire diffraction patterns with reasonable intensity (i.e., the ratio of the interpeak zone to the austenitic (110) peak was approximately 2×10^{-3}). However, since a clear attribution of a single diffraction pattern to a specific phase ϕ of a 20 kHz cycle is crucial, a single exposure should not significantly exceed $1\ \mu\text{s}$. To circumvent this limitation, a frame summation scheme was devised which is illustrated in Fig. 4: Rather than acquiring one single exposure for one specific phase offset position $\Delta\phi_i$, a short frame phase window $\Delta\phi_{\text{fwm}}$ of about $1\ \mu\text{s}$ length at phase position $\Delta\phi_i$ was repeatedly exposed until a cumulative exposure of $t_{\text{exp}, i} = 10\ \text{ms}$ was acquired. This process was repeated for a slightly larger $\Delta\phi_{i+1}$ to obtain $t_{\text{exp}, i+1}$ and so forth, until all phase positions $\Delta\phi$ were covered. For this scheme it is crucial that $\Delta\phi_i$ and $\Delta\phi_{\text{fwm}}$ are accurately timed within a few nanoseconds for every single triggering iteration.

The above scheme was implemented using a NATIONAL INSTRUMENTS multi-function DAQ card (PCIe-6321) running on custom LabVIEW code, generating a (0–5) V trigger signal wired to the detector for gated exposure. Time referencing of

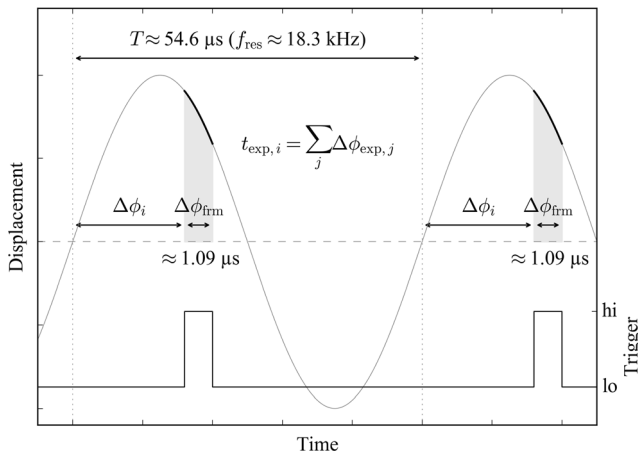


Fig. 4 DAQ and triggering scheme for in situ synchrotron XRD data-acquisition at ultrasonic cycling frequency

the output trigger signal is tied to the cycle generation clock of the ultrasonic fatigue test generator and can be configured to generate j output pulses. The trigger generation sequence starts only after the pulsed ultrasonic vibration has reached its nominal amplitude. If the number of output pulses exceeds the numbers of cycles per pulse, it is split over multiple ultrasonic pulses. The ultrasonic system's resonance frequency is constantly monitored with a continuously running FFT algorithm that is accurate to within 0.1 Hz at the actual 18.3 kHz cycling frequency [33]. The phase-related quantities ($\Delta\phi$, $\Delta\phi_{\text{fm}}$) are set in terms of phase angle, while the corresponding absolute time intervals are continuously calculated from and adjusted for changes in resonance frequency for optimum accuracy of phase attribution. For the current beam configuration a total exposure $t_{\text{exp}, i} = 10$ ms at each of phase offset $\Delta\phi_i$ ($i \in [0, 49]$) was targeted over a frame phase window of 7.2° (i.e., $\Delta\phi_{\text{fm}} \approx 1.09$ μs at ≈ 18.3 kHz resonance frequency), requiring $j = 9174$ individual frames per 10 ms total exposure. The 9174 individual frames were broken up over ten successive ultrasonic pulses of 100 ms duration each.

In addition to the ultrasonic tests, specimens were also cyclically loaded at a low frequency. Exposures of 10 ms were taken at the same 50 phase positions $\Delta\phi_i$ while cycling the specimen at 0.1 Hz. While these measurements set the baseline for comparing scattering patterns at high and low frequency loading, they initially also served a different purpose: Inherent to the ultrasonic equipment's electronic design, the sinusoidal strain signal in the specimen is phase-shifted with respect to the cycle generation clock of the USF equipment by an initially unknown (but constant) amount. By comparing phase resolved observations of lattice deformation at both frequencies, the initial phase offset of the USF equipment can be determined with respect to the known phase of the low-frequency signal. With this, it is possible to pinpoint the phasing i of minimum ($\Delta\phi_{\varepsilon_{\text{min}}}$) and maximum strain ($\Delta\phi_{\varepsilon_{\text{max}}}$), respectively, during an ultrasonic cycle, saving overhead

cycles and time to capture the 48 less relevant positions in between.

In Situ Synchrotron XRD Data

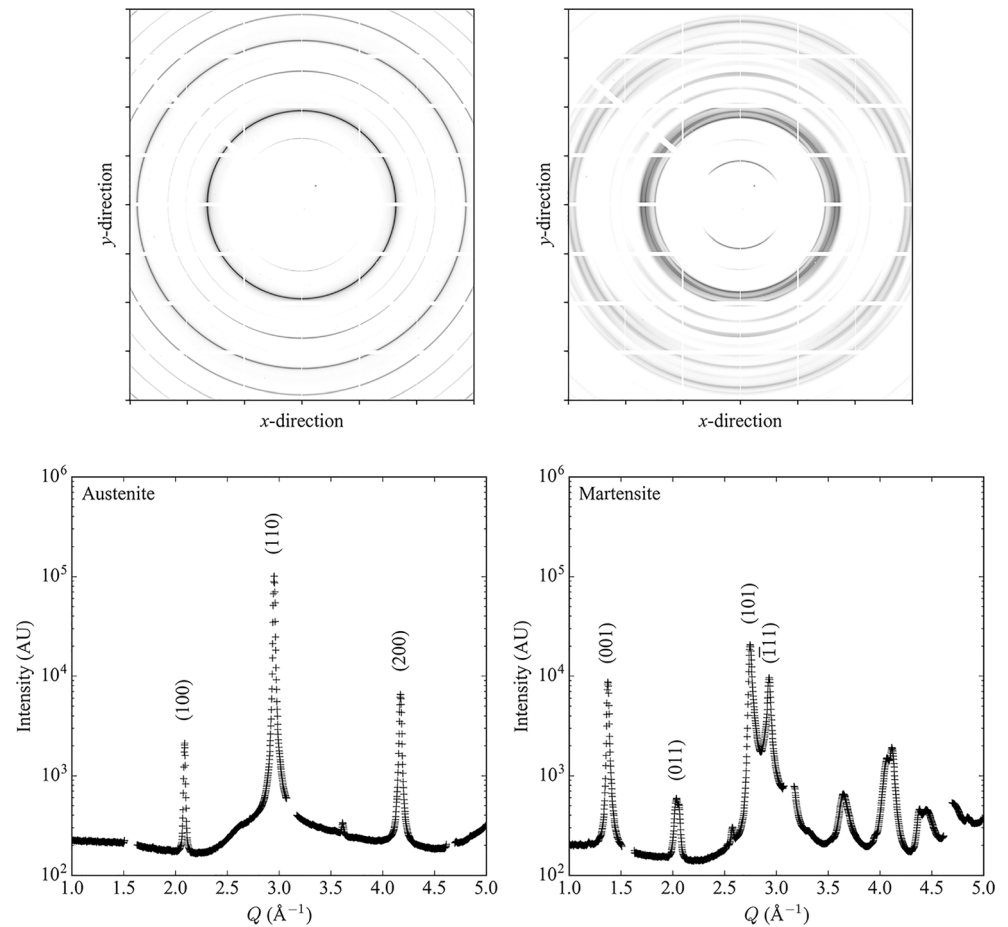
Because the austenite-martensite transformation stress is sensitive to temperature, it is vital to ensure that the X-ray beam does not cause specimen heating. With 86% X-ray transmission through the 0.25 mm thick specimen at 60 keV, in situ temperature measurements with an infrared camera showed no detectable changes in specimen surface temperature with a continuously incident beam on the air-cooled specimen over the duration of one minute. This implies that the mechanical response, phase transformation, and, by extension, diffraction data are unaffected by the X-ray beam.

As detailed in the previous section, a single diffraction pattern was derived from a total exposure of 10 ms. Static diffraction patterns for the investigated Nitinol were acquired in the austenitic (i.e., without any tensile load applied) and in the martensitic state. Figure 5 (top row) shows the raw patterns that allow for a clear distinction between the cubic austenite (B2) (left column) and the monoclinic martensite (B19') (right column) phase. A pronounced directionality (i.e., arcs instead of circles) of some peaks is visible in both patterns, indicating that the specimens were cut (and consequently loaded) in sheet rolling direction that corresponds to the (100) and (200) direction for the austenite, and to (001) for the martensite, respectively. Raw patterns were integrated over the "northern" azimuthal sector between 81° and 99° , as these sectors contain the largest contributions of these peaks. Figure 5 (bottom row) shows the integrated patterns for both phases with the crystallographic directions of the most prominent peaks indicated.

Elastic Deformation at Low and Ultrasonic Frequency

To confirm that the DAQ strategy was sufficiently resolving the ultrasonic vibration signal, lattice deformation Δd was calculated from peak shifts occurring over one full ultrasonic cycle. To this end, the specimen was cycled in tension-tension at the ultrasonic frequency in the fully austenitic state with an amplitude of $\Delta u/2 = 15$ μm (type I), which corresponds to an average strain amplitude of $\Delta\varepsilon/2 = 2.6 \times 10^{-4}$. The mean strain was chosen so that the specimen remained fully austenitic over the whole cycle, but with the minimum strain still in tension (i.e., no compression occurred). The beam was aimed at the center of the gauge section. At a resonance frequency of approximately 18.3 kHz, the strain rate in the center of the gauge section was $\dot{\varepsilon} \approx 7 \times 10^1$ s^{-1} . Patterns were acquired for all 50 phase positions $\Delta\phi_i \in [0^\circ, 352.8^\circ]$. The peak shift was calculated with respect to the specimen at a static mean load. The same procedure was completed for a full loading cycle at a loading

Fig. 5 XRD pattern of austenitic (left column) and martensitic phase (right column); raw patterns (top row) and integrated spectra (bottom row); the most relevant peaks for fitting to derive lattice parameters are indicated

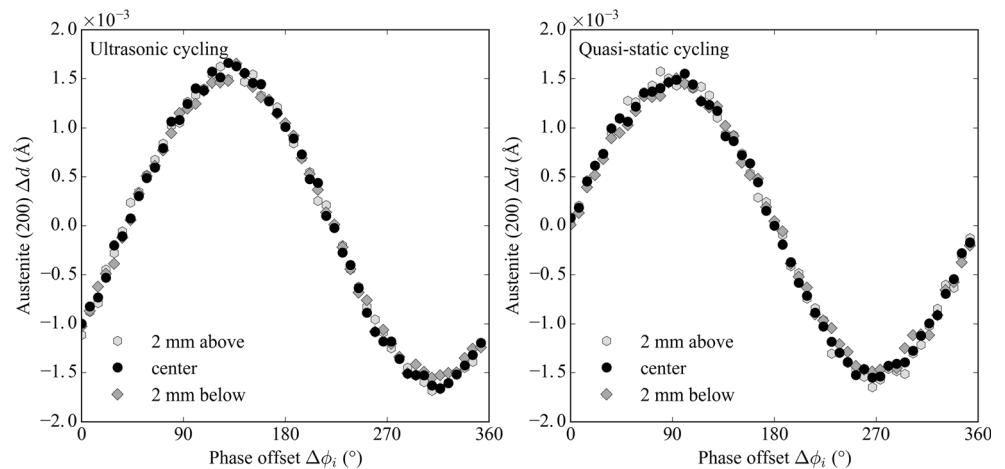


frequency of 0.1 Hz with $\Delta u/2 = 15 \mu\text{m}$ ($\dot{\epsilon} \approx 4 \times 10^{-4} \text{ s}^{-1}$). Figure 6 shows Δd as a function of the phase offset $\Delta\phi_i$ over a full cycle at the ultrasonic frequency (left), and at the 0.1 Hz quasi-static cycling frequency (right). The DAQ strategy is able to resolve lattice deformation due to the sinusoidal vibration reasonably well, both temporally and in magnitude. Coincidentally, the phase offsets for minimum

($\Delta\phi_{\epsilon_{\min}}$) and maximum strain ($\Delta\phi_{\epsilon_{\max}}$), as well as for the two zero crossing positions during one ultrasonic cycle were derived.

The entire procedure was repeated for both ultrasonic and quasi-static loading at 0.1 Hz, at two additional positions: 2 mm above and 2 mm below the center of the gauge section (Figure 6). It is clearly visible that $\Delta d(\Delta\phi_i)$ is virtually identical at all three positions, and also between ultrasonic and

Fig. 6 Phase-resolved shift in B2 (200) lattice spacing $d = 2\pi/Q$ in the fully austenitic specimen with respect to d at tensile mean strain in the center of the gauge section, and 2 mm above and below, respectively, during one full ultrasonic cycle ($f_{\text{res}} \approx 18.3 \text{ kHz}$, $\Delta u/2 = 15 \mu\text{m}$, $\dot{\epsilon} \approx 7 \times 10^1 \text{ s}^{-1}$) (left) and during quasi-static cycling ($f = 0.1 \text{ Hz}$, $\Delta u/2 = 15 \mu\text{m}$, $\dot{\epsilon} \approx 4 \times 10^{-4} \text{ s}^{-1}$) (right)



0.1 Hz loading. This confirms that the assumption of quasi-static behavior during ultrasonic cycling is satisfied, as ultrasonic loading matches loading at 0.1 Hz both in magnitude and uniformity along the specimen.

Nitinol Forward and Reverse R-Phase Transformations during Cycling at Ultrasonic Frequency

During conventional cyclic loading in Nitinol, elastic deformation and phase transformations between austenite, R-phase and martensite are all likely. At ultrasonic strain rates, elastic deformation is expected in the same manner as in conventional loading, and the results presented above experimentally prove this expectation for Nitinol. The same cannot be said about phase transformations, which could possibly be suppressed at high loading rates [17, 20] due to adiabatic heating and consequent increase in transformation stress.

Upon static tensile loading of the fully austenitic specimen (Fig. 2), the R-phase appears in the gauge section at around 200 MPa. When the specimen is cycled around this mean strain, the mass fraction of R-phase in the illuminated volume should increase towards maximum strain and subsequently decrease towards minimum strain.

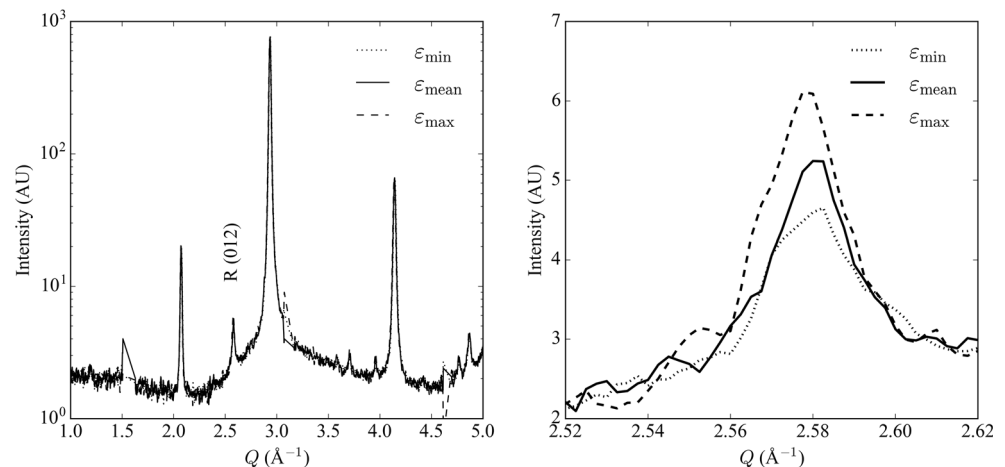
Figure 7 shows integrated diffraction patterns of the R-phase (012) peak that were acquired at maximum, minimum, and mean strain during ultrasonic cycling with $\Delta u/2 = 10 \mu\text{m}$ ($\dot{\epsilon} \approx 5 \times 10^1 \text{ s}^{-1}$ in the center of the gauge section). With increasing strain, the peak height increases in unison with a shift to lower values of Q , while the ratio of the austenitic (110) peak height to the R-phase (012) peak decreases from ≈ 168 at minimum strain to ≈ 121 at maximum strain. The increase in peak height implies a larger mass fraction of R-phase in the illuminated volume, while the shift is a consequence of the lattice deformation during maximum strain. We conclude that the B2 to R-phase transformation,

both forward and reverse, can occur at the very high strain rates during ultrasonic cycling.

Nitinol Forward and Reverse Austenitic-Martensitic Phase Transformations during Cycling at Ultrasonic Frequency

The same concept was employed for investigating forward and reverse transformation to martensite. The specimen was first pre-strained and was then loaded to a point halfway between the lower and the upper plateau stresses, so that the phase distribution across the specimen length would correspond to Fig. 1 (right). The beam was positioned closely below the lower transition zone (i.e., in the austenite). Subsequently, a sufficiently high displacement amplitude was applied to cause hysteretic loading along both plateaus of the stress-strain curve (type II loading; Fig. 2 IIIb). This procedure leads to the experimental difficulty of specimen movement. The upper end of the specimen that is fixed to the resonating ultrasonic horn shows maximum sinusoidal displacement. Towards the lower end that is fixed to the load cell, this movement decreases, however, significant displacement still occurs in the center region of the specimen. With respect to the beam alignment, this means that the location closely below the transition zone, while illuminated by the beam at mean strain, would move upwards under the beam towards maximum strain. Much of the ultrasonic displacement is consumed by elastic deformation of the existing phases, and even if additional martensite were to form, it would not be detected by the beam. Conversely, as the specimen is relaxed to minimum strain, although martensite would be transformed back to austenite, due to the movement of the transition zone additional martensite would be introduced into the beam path. Both effects could impede detection of the forward and reverse transformation. This was overcome by choosing a very high cyclic amplitude of $35 \mu\text{m}$ (equivalent to a global strain amplitude of $\approx 5 \times 10^{-3}$) and aiming the

Fig. 7 R-phase formation during ultrasonic cycling shown at the R-phase (012) peak at minimum, maximum and mean strain during one ultrasonic cycle for the entire acquired Q -range (left) and detailed look at the R-phase (012) peak (right); $\Delta u/2 = 10 \mu\text{m}$, $\dot{\epsilon} \approx 5 \times 10^1 \text{ s}^{-1}$



beam at a point sufficiently far below the transition zone: Even though the transition zone would move away under the beam, the martensitic band would widen so much that it would extend back into the beam at maximum strain, while it would not rebound into the beam at minimum strain. This, however, presents a new difficulty, as the very high amplitudes only yield very short fatigue lifetimes. At 9174 frames per full exposure at each of the 50 phase offsets $\Delta\phi_i$, with each frame accounting for one load cycle, plus overhead cycles during pulse build up the specimen would quickly be destroyed before the acquisition could be completed. This was overcome by only acquiring exposures at the phase positions of minimum and maximum strain, $\Delta\phi_{\varepsilon_{\min}}$ and $\Delta\phi_{\varepsilon_{\max}}$, respectively, that had been obtained by aligning the ultrasonic signal with the known phasing of the 0.1 Hz loading as shown in Fig. 6 (right).

With this it was possible to complete a few subsequent exposures k and $k+1$ at $\Delta\phi_{\varepsilon_{\min}}$ and $\Delta\phi_{\varepsilon_{\max}}$ in an alternating fashion before the specimen fractured. The results are presented in Fig. 8 that shows the Q -range relevant for the martensitic (101) peak. The (101) peak appeared during maximum tensile strain, which shows that martensite formation occurs at the high cyclic strain rate of approximately $\dot{\varepsilon} \approx 2 \times 10^2 \text{ s}^{-1}$ in the center of the gauge section. Further, the martensitic peak disappears during minimum tensile strain. This demonstrates that both the forward and reverse transformation from B2 austenite to the B19' martensite can occur at ultrasonic loading rates.

Discussion

In the present study, we examined strain rate effects on phase transformations in Nitinol by comparing cyclic deformation at ultrasonic loading rates with those at quasi-static rates. Similar work has not been reported earlier in the literature; high strain rate behavior of Nitinol was mostly studied using split-Hopkinson pressure bar (SHPB) setups that exert single impulse loads e.g., [18, 34–36]. These setups often require (cylindrical) specimens of at least several millimeters in thickness and lateral dimensions, and the SHPB does not allow loading of (thin) sheets and wires because impulse transfer requirements cannot be met. Additionally, specimens used in SHPB typically lack stress intensifying shapes i.e., they feature large simultaneously transforming volumes without preordained transforming sections that would localize the stress induced martensite (SIM) transformation. Some degree of pulse shaping is mandatory to achieve at least sectionally constant strain rates. Specimens are loaded from a fully relaxed state to very large strains of up to 24% [18] causing irreversible plastic deformation, which precludes the possibility of investigating fatigue at small cyclic strain amplitudes in specimens under a multi-phase configuration, such as those

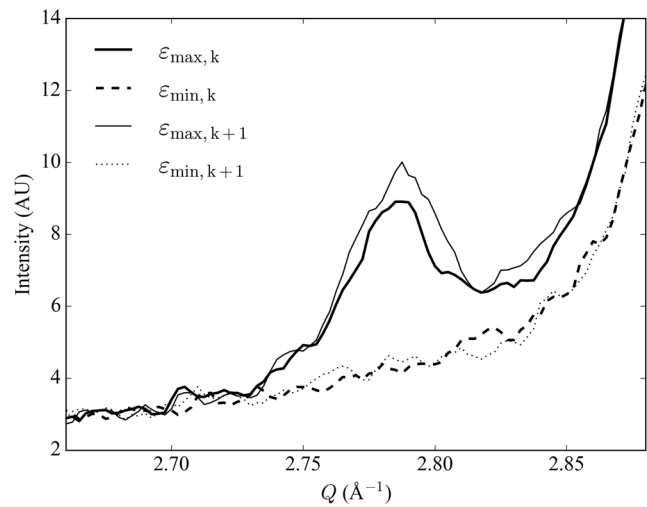


Fig. 8 Austenite - martensite forward and reverse transformation shown by the appearance of the martensitic (101) peak (plotted versus scattering vector Q) during maximum tensile strain ε_{\max} and its disappearance during minimum tensile strain ε_{\min} for subsequent exposures k and $k+1$; $\Delta u/2 = 35 \text{ }\mu\text{m}$, $\dot{\varepsilon} \approx 2 \times 10^2 \text{ s}^{-1}$

that occur during service life of a medical implant like a stent. Even studies that specifically investigate “small strains” [34, 37] focus on single impulse loading of fully relaxed specimens up to several percent strain, a loading configuration that does not resemble actual in service loading conditions. Several studies have reported substantial increases in specimen (surface) temperatures during single impulse loadings at strain rates of the order of 10^3 s^{-1} [18, 20, 34, 38], that are attributed to adiabatic heating, as a multitude of transformation fronts moves through the testing volume. Concomitant shifts of transformation stresses (both forward and reverse) of the order of $\approx 7 \text{ MPa K}^{-1}$ [20] were also observed even at rather low strain rates of about 10^{-3} s^{-1} [39, 40]. This suggests that, at sufficiently high strain rates, stress induced martensite formation could be entirely suppressed [34].

In the present investigation, small cyclic amplitudes of up to $\Delta\varepsilon/2 \approx 5 \times 10^{-3}$ at strain rates of the order of $\dot{\varepsilon} \approx 10^2 \text{ s}^{-1}$ were applied to small sheet specimens in a pre-strained multi-phase state, by means of an adapted USF testing setup. The strain rates were determined by the system’s resonance frequency and the applied displacement amplitude $\Delta u/2$ arising from the sinusoidal loading signal. The aim was to explore the possibility of accelerated fatigue testing of materials intended for medical implant applications under loading conditions relevant to in vivo loading conditions i.e., repeated cyclic loading with small strain amplitudes, versus single impulse loadings with residual plastic deformation.

In the present study, infrared spot measurements (FWHM $\approx 0.5 \text{ mm}$) at the transition zones ($\approx 100 \text{ }\mu\text{m}$ wide; Fig. 2) during cyclic loading with high displacement amplitudes $\Delta u/2 \geq 35 \text{ }\mu\text{m}$ (without forced-air cooling) revealed temperature increases of only

$\Delta T \leq 1$ K. While the real temperature increase is likely underestimated due to the spot size, in contrast to the works above, we did not observe substantial macroscopic heating during cyclic loading of thin dog bone specimens. Temperature increases did not occur despite cyclic martensitic transformation (both, forward and reverse) taking place at the high strain rates of $\dot{\epsilon} \approx 10^2 \text{ s}^{-1}$ (Fig. 8). We suspect the lack of significant temperature increase in the present experiments to be a consequence of the specimen geometry and cyclic loading from a multi-phase state where austenite, R-phase and martensite are all present. The additional transforming volume during cycling loading is only a few μm^3 ; coupled together with the relatively large surface area that allows effective cooling, this limits the concomitant increases in temperature and martensitic transformation stress. In contrast, in previous studies where larger temperature increases were observed in cylindrical specimens of uniform cross section, the transforming volumes were significantly larger [e.g., 18, 34–36]. Additionally, the fact that both the forward and the reverse martensitic transformation are not being suppressed in the present study even at strain rates of $\dot{\epsilon} \approx 10^2 \text{ s}^{-1}$ may also be due to small transforming volumes during cyclic loading. These findings are in line with the crystallography point of view that because the SIM transformation in Nitinol is a displacive volume preserving transformation, it is expected to be rate independent, as long as the temperature is undisturbed by any latent heat release.

The present investigation has strong implications for fatigue testing of Nitinol in the HCF and VHF regime. We showed that the austenite to R-phase transformation occurs during ultrasonic cycling. The amount of R-phase in the predominantly austenitic matrix increases and decreases during an ultrasonic cycle in the same manner as in quasi-static loading. We could also confirm transformation to and from martensite during ultrasonic loading. Since both mechanisms (transformation to R-phase and B19' martensite) that operate at low frequency loading also operate at ultrasonic loading frequencies, one of the principal necessary conditions is met, unlocking the possibility of investigating the fatigue properties of Nitinol in the HCF and VHCF regime. However, it is not yet known if the process of fatigue damage and the associated fatigue lifetimes are equivalent at low and ultrasonic frequencies. Further studies are necessary to investigate how ultrasonic frequency fatigue data can be applied for fatigue prediction of actual components stressed at low frequencies *in vivo*.

Conclusions

In this study, a unique new experimental technique is presented to quantitatively measure strains during high strain rate cyclic deformation, with the primary goal of comparing ultrasonic

and ordinary cyclic loading. The implementation of this method has provided important insights into ultrasonic cyclic loading of Nitinol that are of interest to accelerated fatigue testing of Nitinol medical implants.

- A novel setup for *in situ* synchrotron XRD during ultrasonic cycling of thin sheet specimens of superelastic Nitinol was developed, where the specimens undergo forced vibrations at about 20 kHz cycling frequency. The newly developed technique is capable of applying cyclic strains at high strain rates of the order of $\dot{\epsilon} \approx 10^2 \text{ s}^{-1}$ to superelastic Nitinol dog bone specimens in a pre-strained multi-phase state. It is capable of suppressing macroscopic specimen heating through loading in a pulse-pause sequence and additional forced air cooling.
- An XRD experiment at the ESRF confirmed that the novel setup and DAQ strategy were able to sufficiently resolve lattice deformation during ultrasonic vibrations. Cycling the material in the elastic regime confirmed that the lattice strains produced at ultrasonic loading rates are identical to that observed during quasi-static loading.
- The same deformation mechanisms were activated at ordinary (0.1 Hz, $\dot{\epsilon} \approx 10^{-3} \text{ s}^{-1}$) and ultrasonic (20 kHz, $\dot{\epsilon} \approx 10^2 \text{ s}^{-1}$) loading rates namely, the forward and reverse transformation from austenite to martensite through the intermediate R-phase.
- The XRD experiment addresses the general applicability of the ultrasonic fatigue testing technique to Nitinol. Further testing is necessary to compare low frequency and ultrasonic testing at high amplitudes to unlock the possibility of investigating Nitinol fatigue behavior in the HCF and VHF regime with the ultrasonic technique.

Acknowledgements This work was supported by Medtronic plc., MN, USA, through a grant to the University of Natural Resources and Life Sciences, Vienna, Austria. The authors would also like to thank their colleague R. Schuller at the Institute of Physics and Materials Science for his continued support and assistance.

Funding Information Open access funding provided by University of Natural Resources and Life Sciences Vienna (BOKU).

Open Access This article is licensed under a Creative Commons Attribution 4.0 International License, which permits use, sharing, adaptation, distribution and reproduction in any medium or format, as long as you give appropriate credit to the original author(s) and the source, provide a link to the Creative Commons licence, and indicate if changes were made. The images or other third party material in this article are included in the article's Creative Commons licence, unless indicated otherwise in a credit line to the material. If material is not included in the article's Creative Commons licence and your intended use is not permitted by statutory regulation or exceeds the permitted use, you will need to obtain permission directly from the copyright holder. To view a copy of this licence, visit <http://creativecommons.org/licenses/by/4.0/>.



References

- Wang FE, Buehler WJ, Pickart SJ (1965) Crystal structure and a unique “martensitic” transition of TiNi. *J Appl Phys* 36(10):3232–3239. <https://doi.org/10.1063/1.1702955>
- Buehler WJ, Gilfrich JV, Wiley RC (1963) Effect of low-temperature phase changes on the mechanical properties of alloys near composition TiNi. *J Appl Phys* 34(5):1475–1477. <https://doi.org/10.1063/1.1729603>
- Duerig T, Pelton A, Stöckel D (1999) An overview of nitinol medical applications. *Mat Sci Eng A-Struct* 273–275:149–160. [https://doi.org/10.1016/s0921-5093\(99\)00294-4](https://doi.org/10.1016/s0921-5093(99)00294-4)
- Duerig TW, Tolomeo DE, Wholey M (2000) An overview of superelastic stent design. *Minim Invasiv Ther* 9(3–4):235–246. <https://doi.org/10.1080/13645700009169654>
- Robertson SW, Pelton AR, Ritchie RO (2012) Mechanical fatigue and fracture of Nitinol. *Int Mater Rev* 57(1):1–36. <https://doi.org/10.1179/1743280411y.0000000009>
- Robertson SW, Stankiewicz JM, Gong XY, Ritchie RO (2003) Cyclic fatigue of NiTiNOL, International Conference on Shape Memory and Superelastic Technologies, ASM International, Baden-Baden, Germany, pp. 79–88
- McKelvey AL, Ritchie RO (1999) Fatigue-crack propagation in Nitinol, a shape-memory and superelastic endovascular stent material. *J Biomed Mater Res* 47(3):301–308. [https://doi.org/10.1002/\(sici\)1097-4636\(19991205\)47:3<301::aid-jbm3>3.0.co;2-h](https://doi.org/10.1002/(sici)1097-4636(19991205)47:3<301::aid-jbm3>3.0.co;2-h)
- Stankiewicz JM, Robertson SW, Ritchie RO (2007) Fatigue-crack growth properties of thin-walled superelastic austenitic Nitinol tube for endovascular stents. *J Biomed Mater Res A* 81(3):685–691. <https://doi.org/10.1002/jbm.a.31100>
- Lin Z, Pike K, Zipse A, Schlun M (2010) Nitinol fatigue investigation on stent-finish specimens using tension-tension method. *J Mater Eng Perform* 20(4–5):591–596. <https://doi.org/10.1007/s11665-010-9792-0>
- Pelton AR, Schroeder V, Mitchell MR, Gong XY, Barney M, Robertson SW (2008) Fatigue and durability of Nitinol stents. *J Mech Behav Biomed* 1(2):153–164. <https://doi.org/10.1016/j.jmbbm.2007.08.001>
- Scirè Mammano G, Dragoni E (2014) Functional fatigue of Ni–Ti shape memory wires under various loading conditions. *Int J Fatigue* 69:71–83. <https://doi.org/10.1016/j.ijfatigue.2012.03.004>
- Otsuka K, Ren X (2005) Physical metallurgy of Ti–Ni-based shape memory alloys. *Prog Mater Sci* 50(5):511–678. <https://doi.org/10.1016/j.pmatsci.2004.10.001>
- Mahtabi MJ, Shamsaei N, Mitchell MR (2015) Fatigue of Nitinol: the state-of-the-art and ongoing challenges. *J Mech Behav Biomed Mater* 50:228–254. <https://doi.org/10.1016/j.jmbbm.2015.06.010>
- Pelton A, Duerig TW, Gong XY (2003) Fatigue testing of diamond-shaped specimens, International Conference on Shape Memory and Superelastic Technologies, ASM International, Monterey, US, pp. 1–8
- Pelton AR, Fino-Decker J, Vien L, Bonsignore C, Saffari P, Launey M, Mitchell MR (2013) Rotary-bending fatigue characteristics of medical-grade Nitinol wire. *J Mech Behav Biomed* 27:19–32. <https://doi.org/10.1016/j.jmbbm.2013.06.003>
- Kang G, Song D (2015) Review on structural fatigue of NiTi shape memory alloys: pure mechanical and thermo-mechanical ones. *Theor Appl Mech Lett* 5(6):245–254. <https://doi.org/10.1016/j.taml.2015.11.004>
- Shaw JA, Kyriakides S (1995) Thermomechanical aspects of Niti. *J Mech Phys Solids* 43(8):1243–1281. [https://doi.org/10.1016/0022-5096\(95\)00024-d](https://doi.org/10.1016/0022-5096(95)00024-d)
- Adharapurapu RR, Jiang F, Vecchio KS, Gray GT (2006) Response of NiTi shape memory alloy at high strain rate: a systematic investigation of temperature effects on tension–compression asymmetry. *Acta Mater* 54(17):4609–4620. <https://doi.org/10.1016/j.actamat.2006.05.047>
- Nemat-Nasser S, Guo W-G (2006) Superelastic and cyclic response of NiTi SMA at various strain rates and temperatures. *Mech Mater* 38(5–6):463–474. <https://doi.org/10.1016/j.mechmat.2005.07.004>
- Shaw JA, Kyriakides S (1997) On the nucleation and propagation of phase transformation fronts in a NiTi alloy. *Acta Mater* 45(2):683–700. [https://doi.org/10.1016/s1359-6454\(96\)00189-9](https://doi.org/10.1016/s1359-6454(96)00189-9)
- Paranjape HM, Paul PP, Amin-Ahmadi B, Sharma H, Dale D, Ko JYP, Chumlyakov YI, Brinson LC, Stebner AP (2018) In situ, 3D characterization of the deformation mechanics of a superelastic NiTi shape memory alloy single crystal under multiscale constraint. *Acta Mater* 144:748–757. <https://doi.org/10.1016/j.actamat.2017.11.026>
- Robertson SW, Mehta A, Pelton AR, Ritchie RO (2007) Evolution of crack-tip transformation zones in superelastic Nitinol subjected to in situ fatigue: a fracture mechanics and synchrotron X-ray microdiffraction analysis. *Acta Mater* 55(18):6198–6207. <https://doi.org/10.1016/j.actamat.2007.07.028>
- Sedmak P, Pilch J, Heller L, Kopecek J, Wright J, Sedlak P, Frost M, Sittner P (2016) Grain-resolved analysis of localized deformation in nickel-titanium wire under tensile load. *Science* 353(6299):559–562. <https://doi.org/10.1126/science.aad6700>
- Sedmak P, Šittner P, Pilch J, Curfs C (2015) Instability of cyclic superelastic deformation of NiTi investigated by synchrotron X-ray diffraction. *Acta Mater* 94:257–270. <https://doi.org/10.1016/j.actamat.2015.04.039>
- Stebner AP, Paranjape HM, Clausen B, Brinson LC, Pelton AR (2015) In situ neutron diffraction studies of large monotonic deformations of Superelastic Nitinol. *Shap Mem Superelasticity* 1(2):252–267. <https://doi.org/10.1007/s40830-015-0015-2>
- Ling HC, Roy K (1981) Stress-induced shape changes and shape memory in the R and Martensite transformations in Equiatomic NiTi. *Metall Trans A* 12(12):2101–2111. <https://doi.org/10.1007/BF02644180>
- Schuller R, Fitzka M, Irrasch D, Tran D, Pennings B, Mayer H (2015) VHCF properties of nitrided 18Ni maraging steel thin sheets with different Co and Ti content. *Fatigue Fract. Eng. M.* 38(5):518–527. <https://doi.org/10.1111/ffe.12251>
- Mayer H (2016) Recent developments in ultrasonic fatigue. *Fatigue Fract Eng M* 39(1):3–29. <https://doi.org/10.1111/ffe.12365>
- Fitzka M, Catoor D, Irrasch D, Reiterer M, Mayer H (2017) Fatigue testing of thin CoNiCr wire up to 10^{10} cycles. *Int J Fatigue* 98:92–100. <https://doi.org/10.1016/j.ijfatigue.2017.01.027>
- Mehta A, Gong XY, Imbeni V, Pelton AR, Ritchie RO (2007) Understanding the deformation and fracture of Nitinol endovascular stents using in situ synchrotron X-ray microdiffraction. *Adv Mater* 19(9):1183–1186. <https://doi.org/10.1002/adma.200601916>
- Thayer TA, Bagby MD, Moore RN, DeAngelis RJ (1995) X-ray diffraction of nitinol orthodontic arch wires. *Am J Orthod Dentofac* 107(6):604–612. [https://doi.org/10.1016/S0889-5406\(95\)70103-6](https://doi.org/10.1016/S0889-5406(95)70103-6)
- Iijima M, Ohno H, Kawashima I, Endo K, Brantley WA, Mizoguchi I (2002) Micro X-ray diffraction study of superelastic nickel–titanium orthodontic wires at different temperatures and stresses. *Biomaterials* 23(8):1769–1774. [https://doi.org/10.1016/s0142-9612\(01\)00303-9](https://doi.org/10.1016/s0142-9612(01)00303-9)
- Mayer H, Fitzka M, Schuller R (2013) Constant and variable amplitude ultrasonic fatigue of 2024-T351 aluminium alloy at different

- load ratios. *Ultrasonics* 53(8):1425–1432. <https://doi.org/10.1016/j.ultras.2013.02.012>
34. Nemat-Nasser S, Yong Choi J, Guo W-G, Isaacs JB, Taya M (2005) High strain-rate, small strain response of a NiTi shape-memory alloy. *J Eng Mater Technol* 127(1). <https://doi.org/10.1115/1.1839215>
35. Wang JJ, Guo WG (2012) Pseudo-elastic behavior of NiTi SMA under the quasi-static and the impact cyclic tests. *Adv Mater Res* 560-561:13–19. <https://doi.org/10.4028/www.scientific.net/AMR.560-561.13>
36. Liu Y, Xie Z, Van Humbeeck J, Delaey L (1998) Asymmetry of stress–strain curves under tension and compression for NiTi shape memory alloys. *Acta Mater* 46(12):4325–4338. [https://doi.org/10.1016/s1359-6454\(98\)00112-8](https://doi.org/10.1016/s1359-6454(98)00112-8)
37. Lin P-h, Tobushi H, Tanaka K, Hattori T, Ikai A (1996) Influence of strain rate on deformation properties of TiNi shape memory alloy. *JSME International Journal Ser. A, Mechanics and Material Engineering* 39(1):117–123. https://doi.org/10.1299/jsmea1993.39.1_117
38. Miller DA, Thissell WR, Macdougall DAS (2000) Dynamic tensile plasticity and damage evolution in shape-memory Ni-Ti, *Le Journal de Physique IV* 10(PR9), Pr9–341-Pr9–346, doi:<https://doi.org/10.1051/jp4:2000957>
39. Leo PH, Shield TW, Bruno OP (1993) Transient heat transfer effects on the pseudoelastic behavior of shape-memory wires. *Acta Metall Mater* 41(8):2477–2485. [https://doi.org/10.1016/0956-7151\(93\)90328-P](https://doi.org/10.1016/0956-7151(93)90328-P)
40. Tobushi H, Shimeno Y, Hachisuka T, Tanaka K (1998) Influence of strain rate on superelastic properties of TiNi shape memory alloy. *Mech Mater* 30(2):141–150. [https://doi.org/10.1016/S0167-6636\(98\)00041-6](https://doi.org/10.1016/S0167-6636(98)00041-6)

Publisher's Note Springer Nature remains neutral with regard to jurisdictional claims in published maps and institutional affiliations.